nature communications

Article

https://doi.org/10.1038/s41467-025-60715-3

Mechanochemical ammonia synthesis enhanced by silicon nitride as a defect-inducing physical promoter

Received: 27 March 2025

Accepted: 2 June 2025

Jae Seong Lee[1,6], **Sooyeon Kim**[2,3,6], **Seung-Hyeon Kim**[1], **Jae-Hoon Baek**[1], **Jeong-Min Seo**[4], **Se Jung Lee**[1], **Changqing Li**[1], **Runnan Guan**[1], **Boo-Jae Jang**[1], **Gao-Feng Han**[5] ✉, **Sang Soo Han**[2] ✉ & **Jong-Beom Baek**[1] ✉

By enabling ammonia synthesis under near ambient conditions, mechanochemistry provides a paradigm shift, a new decentralized production method that avoids the high temperature (above 400 °C) and high pressure (above 200 bar) requirements of the centralized Haber-Bosch process. Leveraging the principles of mechanochemistry and its dynamic reaction environment, we hypothesize that inducing high-density defects on iron (Fe) catalyst can amplify catalytic activity by increasing initial state and adsorption capacity. In this study, we introduce a novel mechanochemical ammonia synthesis method utilizing silicon nitride (Si_3N_4) as a defect-inducing physical promoter. The physical properties of Si_3N_4 make it an ideal candidate to more efficiently generate active surfaces on Fe catalyst via mechanochemical actions. The Fe catalyst with Si_3N_4 (3.0 at%) promoter achieves an ammonia concentration 5.6-fold higher than unpromoted Fe, while maintaining substantial stability. This research not only establishes a promising pathway for low-energy ammonia production but also provides insights into dynamic defect engineering strategies for catalytic systems.

Ammonia (NH_3) synthesis is a critical industrial process, with demand primarily driven by its fundamental use in agricultural fertilizers and other high-value chemical industries[1–3]. Ammonia synthesis ($N_2 + 3H_2 \rightarrow 2NH_3$) is a thermodynamically exothermic reaction ($\Delta H = -92\ \mathrm{kJ\ mol^{-1}}$)[4], which theoretically suggests that decreasing the process temperature would be advantageous for ammonia conversion. For kinetic reasons, however, the conventional Haber-Bosch process typically operates under extremely harsh conditions, at high temperature (above 400 °C) and pressure (above 200 bar), which results in not only significant energy consumption and environmental impact, but low conversion[2,5–9]. As a result, the thermochemical Haber-Bosch process requires large-scale centralized manufacturing facilities. In recent years, interest has grown in using ammonia as an efficient hydrogen carrier for the emerging hydrogen economy[10–14]. Hydrogen energy is increasingly recognized as a sustainable and clean energy source that can significantly reduce greenhouse gas emissions and dependence on fossil fuels[15]. However, storing and transporting hydrogen poses significant challenges. Ammonia, with its high hydrogen content (17.6 wt%) and relatively low liquefaction temperature (−33 °C at 1 atm)[16–18], offers a viable solution for hydrogen storage and transportation.

---

[1] School of Energy and Chemical Engineering, Center for Dimension-Controllable Organic Frameworks, Ulsan National Institute of Science and Technology (UNIST), Ulsan, Republic of Korea. [2] Computational Science Research Center, Korea Institute of Science and Technology (KIST), Seoul, Republic of Korea. [3] Department of Chemistry, Myongji University, Yongin, Republic of Korea. [4] SKKU Advanced Institute of Nanotechnology (SAINT), Sungkyunkwan University, Suwon, Republic of Korea. [5] Key Laboratory of Automobile Materials (Jilin University), Ministry of Education, and School of Materials Science and Engineering, Jilin University, Changchun, PR China. [6] These authors contributed equally: Jae Seong Lee, Sooyeon Kim. ✉ e-mail: gfhan@jlu.edu.cn; sangsoo@kist.re.kr; jbbaek@unist.ac.kr

Mechanochemical ammonia synthesis has emerged as a promising decentralized technique[19–24], offering an alternative to traditional centralized methods. Utilizing mechanical energy to drive chemical reactions under near ambient conditions, the method reduces the overall energy footprint. In our previous study, we introduced potassium (K) as a chemical promoter to enhance ammonia yield when using an iron (Fe) catalyst[20]. However, potassium's high sensitivity to air can pose challenges in industrial scale applications. Therefore, developing a safer and less sensitive promoter with similar performance is crucial for practical use. Given the principles and dynamic reaction environments of mechanochemistry, generating high-density defects can raise initial state (IS) and thus potentially enhance catalytic activity[25–29].

In this study, we explore the use of silicon nitride (Si_3N_4) as a physical promoter to the Fe catalyst for mechanochemical ammonia synthesis. The work aims to elucidate the mechanistic role of Si_3N_4. Si_3N_4 is a robust ceramic material known for its high hardness, low sinterability, and high oxidation resistance[30], making it a promising candidate for generating high-density defects on an Fe catalyst. Through defect engineering, Si_3N_4 facilitates hydrogenation processes by enhancing the catalytic activity of Fe, which can improve hydrogen adsorption and activation, thereby promoting NH_3 efficiency. Consequently, Si_3N_4 is attractive both because of its technical advantages and its potential role in addressing pressing sustainability challenges.

Crystalline silicon modules currently comprise over 90% of globally installed solar power capacity, and the exponential growth of silicon-based photovoltaic (PV) waste presents a significant environmental concern[31]. Current projections indicate an accumulation of 49 million tons of PV waste by 2050, making the repurposing of silicon waste increasingly crucial. Our approach offers a unique solution by potentially utilizing silicon from PV waste for Si_3N_4 production, thereby simultaneously addressing ammonia synthesis efficiency and waste management challenges. This innovative approach creates a bridge between renewable energy waste management and sustainable chemical manufacturing, realizing principles of the circular economy and industrial symbiosis.

Adding only 3.0 at% of Si_3N_4 to Fe during mechanochemical ammonia synthesis resulted in an approximately 5.6-fold improvement compared to using the Fe catalyst alone. The high-adsorption capacity of the Fe catalyst with high-density defects, induced by the hard physical Si_3N_4 promoter, could be responsible for the enhanced catalytic performance in the first nitrogen dissociation step (Fig. 1). Si_3N_4 also creates a diverse surface landscape with multiple hydrogen adsorption sites, potentially advantageous for the second hydrogenation step into ammonia.

By exploiting the synergistic effects of dynamic mechanical forces and physical promoters including Si_3N_4, it is possible to design new catalytic systems that operate under milder conditions, thereby reducing the energy footprint associated with traditional high-temperature and high-pressure ammonia synthesis. These findings pave the way for the development of next-generation catalysts that leverage mechanochemical principles for efficient and sustainable ammonia production.

Results

Si-based promoter comparison

Prior to conducting the main experiments, we performed control experiments to determine whether the lattice nitrogen in Si_3N_4 directly participates in the ammonia synthesis reaction. In one control experiment, Si_3N_4 was used as a physical promoter and mechanochemically treated in the presence of hydrogen (H_2) without a Fe catalyst. The second control experiment was carried out with Fe and Si_3N_4 (Si_3N_4/Fe) in the presence of argon (Ar) and H_2 under identical conditions. Both control experiments yielded no detectable ammonia concentrations (less than 1 ppm) (Supplementary Figs. 1, 2). The results indicated that the Si_3N_4 was not a nitrogen source or catalyst for ammonia synthesis, but a physical promoter. These insights underscore the mechanistic role of the Si_3N_4 promoter in facilitating N_2 dissociation and H_2 activation on the Fe catalyst under milder conditions.

Exploring mechanochemical ammonia synthesis, a comparative analysis of Si-based promoters—Si_3N_4, silicon carbide (SiC), and silicon oxide (SiO_2)—alongside a Fe catalyst was conducted under identical reaction conditions (Fig. 2a). Si_3N_4 emerged as the superior promoter, enhancing both ammonia yield and selectivity (Supplementary Figs. 3, 4). Despite the favorable physical properties of SiC, its catalytic performance was suboptimal due to the formation of methane byproduct. SiO_2 exhibited a beneficial effect on ammonia yield, likely due to improved thermal stability and the dispersion of active Fe species, despite the general detrimental effect of oxygen on metal catalysts[32]. N_2 dissociation studies, crucial for elucidating the ammonia synthesis mechanism, revealed a strong correlation with NH_3 synthesis activity. Si_3N_4 promoted Fe (Si_3N_4/Fe) demonstrated high N≡N triple bond activation capacity, while the SiC and SiO_2 systems showed diminished performance. Notably, our investigation using high-purity Fe balls revealed enhanced selectivity for NH_3 production with significantly reduced methane formation (Supplementary Fig. 5). While trace amounts of CH_4 were still detected, it could be attributed to residual carbon in the reaction vessel. These findings suggest that the chemical nature of the promoter significantly impacts its interaction with N_2 molecules and, consequently, the overall catalytic performance of mechanochemical ammonia synthesis.

The phase dependence of Si_3N_4 was also investigated to determine the difference between alpha (α-), beta (β-), and amorphous Si_3N_4 (am-Si_3N_4). Among tested promoters, β-Si_3N_4 demonstrated the highest physical promoter effect for both the nitrogen dissociation and subsequent hydrogenation steps, whereas am-Si_3N_4 exhibited a lower yield due to its high surface area covering a significant portion of the Fe active sites (Supplementary Figs. 6, 7). Consequently, all of the following experiments were conducted with β-Si_3N_4, unless specified.

Next, we investigated the optimal loading amount of Si_3N_4 promoter. The catalytic activity increased with Si_3N_4 loading up to 3.0 at%, as evidenced from the increased amount of dissociated N_2 (Supplementary Fig. 8a) and synthesized NH_3 (Fig. 2b). However, in contrast to using potassium (K) as a chemical promoter (electron donor to Fe)[20], the activity of Si_3N_4/Fe sharply declined when the Si_3N_4 loading exceeded 3.0 at%, which could be attributed to a decrease in the number of Fe active sites covered by Si_3N_4. Therefore, the optimal promoter loading turned out to be 3.0 at% for both the N_2 adsorption (N_2 dissociation) and hydrogenation (into NH_3) steps. Unless otherwise specified, all subsequent experiments were conducted using an Si_3N_4 loading of 3.0 at%.

In-depth performance evaluation

The kinetics of the two-step mechanochemical ammonia synthesis, involving N_2 dissociation and subsequent hydrogenation into ammonia, were first investigated for optimization. As shown in Fig. 2c, the optimum rotation speed for N_2 adsorption was found to be 450 r.p.m., irrespective of the presence of Si_3N_4. The catalytic activity exhibited a volcano-type dependence on rotation speed. The high hardness and abrasion resistance of Si_3N_4 enabled the creation of more defects on Fe under dynamic reaction conditions, resulting in an improved N_2 dissociation performance. The Si_3N_4/Fe and Fe catalytic systems both had the highest surface-adsorbed nitrogen (N*) fixation rate at 500 r.p.m. (Supplementary Fig. 9a). However, there was a marginal difference in N_2 absorption rates between 450 and 500 r.p.m. for Si_3N_4/Fe and Fe.

The amounts of N_2 dissociation with respect to milling time were also investigated for both Si_3N_4/Fe and Fe catalytic systems at a fixed rotation speed of 450 r.p.m. Following an initial stabilization period of 5 h, Si_3N_4/Fe demonstrated linear N_2 adsorption kinetics over time, suggesting a repeated defect formation that enabled continuous N_2

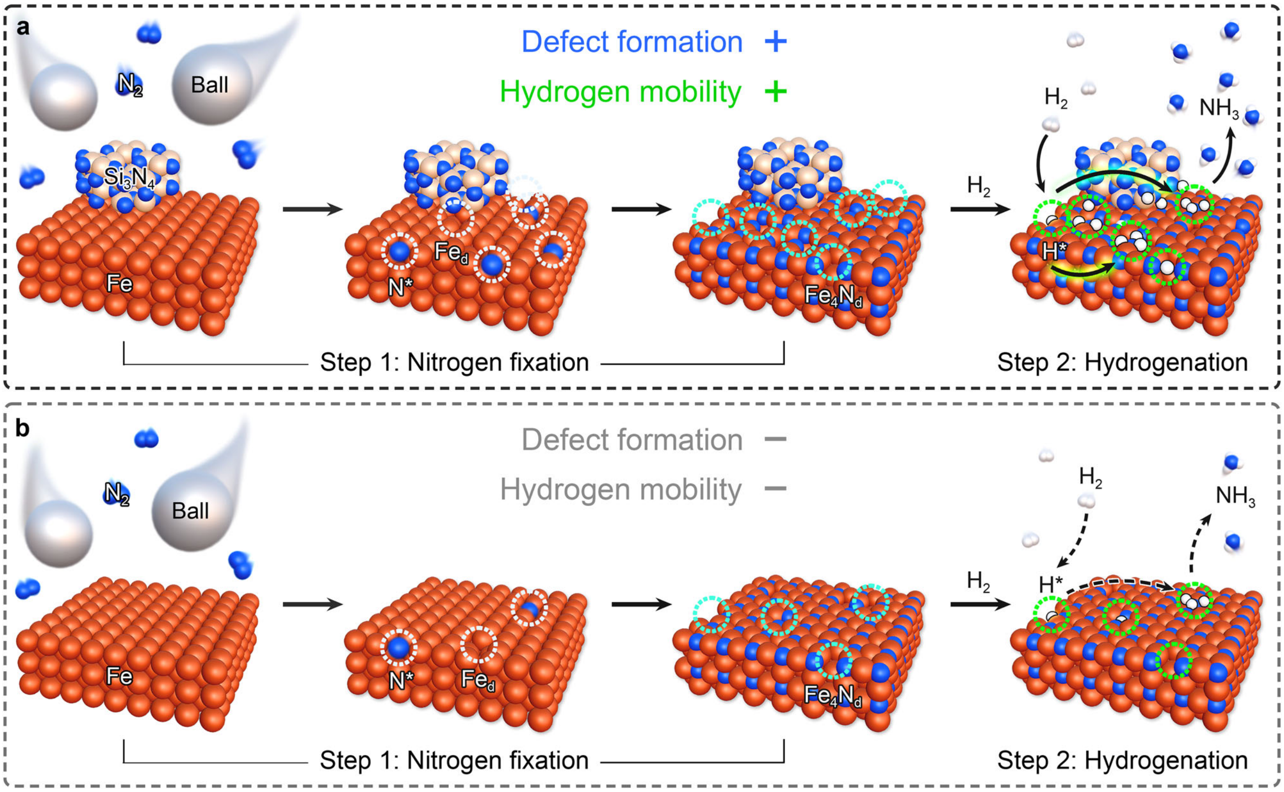

Fig. 1 | Mechanistic investigation of defect-induced promotion in mechanochemical ammonia synthesis. Proposed reaction pathway illustration of **a** Si_3N_4/Fe and **b** unpromoted Fe catalysts. Color code: Fe−orange, Si− apricot, N−blue, H−white, and ball−gray.

cleavage. (Fig. 2d and Supplementary Fig. 9b). Conversely, Fe showed natural logarithmic adsorption, suggesting saturation with milling time. Si_3N_4/Fe demonstrated improved catalytic performance, and dissociating 20 mmol N_2 required much less time (21.9 h) than Fe (54.0 h). It is noteworthy that the ball-milling method typically exhibits an induction period before the reaction starts, as the Fe catalyst requires activation by comminution. The induction time (1.3 h) required for Si_3N_4/Fe was also much shorter than Fe (2.8 h). Furthermore, the energy efficiency of Si_3N_4/Fe in the nitrogen dissociation step was 2.5 times higher than Fe (Supplementary Fig. 10a). These findings underscore the role of Si_3N_4 as a physical promoter that enhances the performance of mechanochemical ammonia synthesis.

Mechanochemical hydrogenation into ammonia (the second step), which was revealed to be an endothermic reaction[19,20,33], was conducted at the rotation speed of 500 r.p.m. Si_3N_4/Fe exhibited different reaction kinetics from Fe: the natural logarithm of the hydrogenation rate linearly decayed with the natural logarithm of reaction time (Fig. 2e). This is in contrast to the unpromoted Fe, where the natural logarithm of the hydrogenation rate linearly decayed with time (Supplementary Fig. 11). The absolute decay constant was determined to be 2.22 for Si_3N_4/Fe, much higher than for Fe (0.25). The difference in the hydrogenation rates of the two catalytic systems could originate with distinct hydrogen kinetics. As hydrogenation progressed, the ammonia yield rate exponentially dropped in both systems. A single hydrogenation cycle proved insufficient to fully dissociated N* species on FeN* into NH_3, most likely because of decreasing N* concentration as the reaction progressed. Further comparative experiments and stability tests were performed using the chemical promoter potassium (K). In the initial ammonia synthesis cycle, no significant differences were observed between the catalytic performance of the physical promoter (Si_3N_4) and the chemical promoter (K) (Supplementary Fig. 12a). However, over subsequent cycles, both the physically promoted Si_3N_4/Fe and the unpromoted Fe catalysts maintained stable performance, whereas the chemically promoted FeK exhibited a substantial decay in activity (Fig. 2f and Supplementary Fig. 12b).

Both total reactor pressure and hydrogen content were reduced after hydrogenation as the Si_3N_4 content was increased (Supplementary Fig. 8b, c). This result suggests that H_2 cleavage preferentially occurred on the Si_3N_4 surface in the form of adsorbed hydrogen adatom (H*) species, and then transferred to the N* species on the in-situ formed metastable iron nitride (Fe-N) into ammonia. Moreover, the Si_3N_4/Fe system yielded 28.7 mmol kWh^{-1} ammonia, a value 5.6 times higher than Fe (5.1 mmol kWh^{-1}) (Supplementary Fig. 10b). This substantial improvement in energy efficiency highlights the pivotal role of Si_3N_4 in the hydrogenation step, which is the rate-determining step (RDS) in this mechanochemical process. The increased hydrogen mobility contributes to the kinetics for the hydrogenation step, enabling efficient ammonia synthesis at lower temperatures.

Defect mediated catalyst characterization

Figure 3a shows X-ray diffraction (XRD) patterns of the nitrogenated Si_3N_4/Fe (denoted as Si_3N_4/FeN*), which exhibited a shift towards lower angles compared to the pristine Fe powder (COD 96-900-2673). This peak shift in the XRD patterns indicates lattice expansion. It can be attributed to the diffusion of dissociated N* moieties into the Fe matrix, occupying interstitial positions. The mobility of N* atoms within the lattice implies that they are diffused into the Fe matrix, providing diverse active sites for efficient reaction. Si_3N_4/FeN* demonstrated a broader full width at half maximum of 2.75° compared to the pristine Fe (0.311°), indicating a substantial reduction in grain size (Si_3N_4/FeN*: 3.26 nm, pristine Fe: 28.88 nm). This grain size reduction is highly beneficial for ammonia synthesis, as it provides a larger surface area for efficient nitrogen uptake and an increased IS, relatively decreasing the activation barrier.

The addition of Si_3N_4 had a pronounced effect on grain size reduction, as evidenced by comparing Si_3N_4/FeN* with FeN* (FeN*

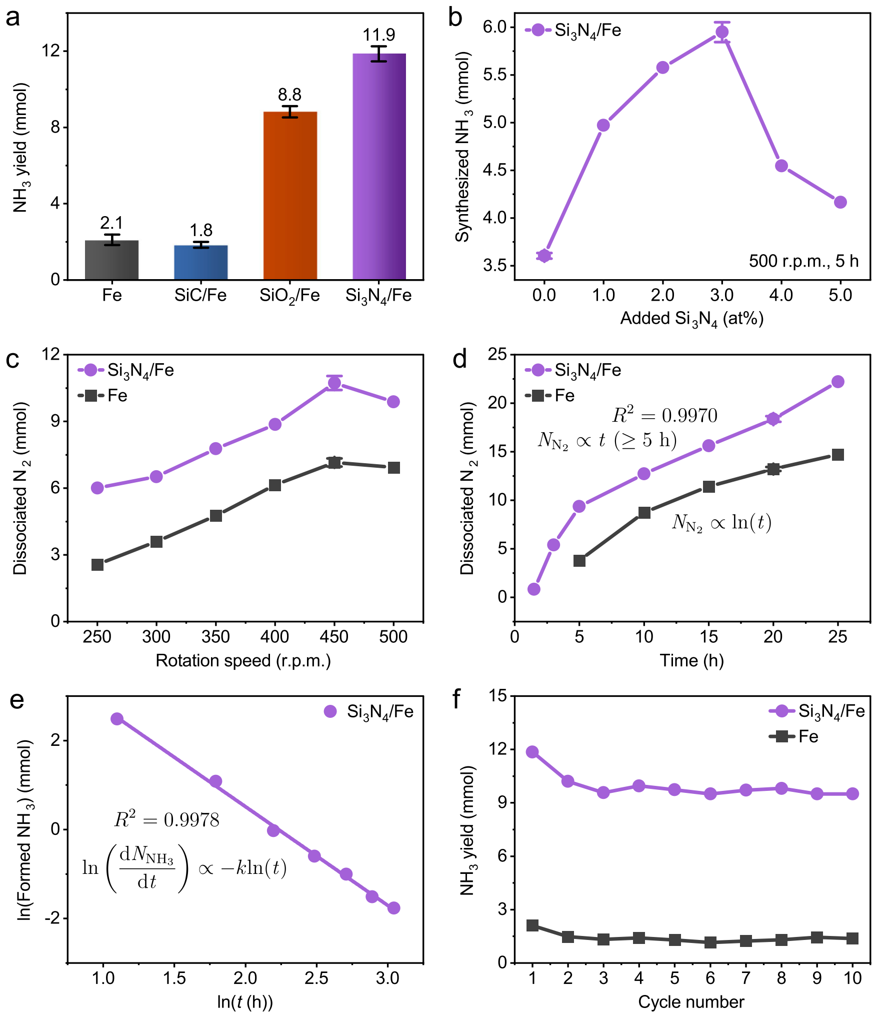

Fig. 2 | Evaluation of physical promoter performance during mechanochemistry. a NH_3 yield from various silicon-based promoters added at the same loading amount (3.0 at%). N_2 dissociation was conducted at 9 bar for 20 h, followed by hydrogenation at 9 bar for 3 h. **b** Synthesized ammonia at varying amounts of Si_3N_4 for a rotation speed of 500 r.p.m. and a milling time of 5 h. **c** The amount of dissociated N_2 as a function of rotation speed after 240,000 total rotating cycles. **d** The dissociated N_2 by ball-milling time at 450 r.p.m. N_2 adsorption exhibits a linear dependence on ball-milling time for Si_3N_4/Fe, while N_2 dissociation follows a linear relationship with the natural logarithm of time [ln(*t*)] for Fe. **e** The natural logarithm of synthesized NH_3 vs. the natural logarithm of milling time for Si_3N_4/Fe. **f** Stability test results. Error bars represent the standard deviation of at least three independent experiments.

1.14°, 7.86 nm, Supplementary Fig. 14). The presence of Si_3N_4 effectively suppresses grain growth through the pinning effect of N* atoms[34]. The regenerated Si_3N_4/Fe (denoted as re-Si_3N_4/Fe) exhibited XRD peaks at angles similar to the pristine Fe powder. This suggests effective catalyst regeneration (comminution ↔ aggregation) with retention of structural integrity for continuous use. In addition, the grain size of the regenerated Si_3N_4/Fe (2.33°, 3.85 nm) remained smaller than the regenerated Fe (re-Fe, 1.31°, 6.85 nm), suggesting that Si_3N_4 was more effectively pulverized than the Fe catalyst and experienced less deactivation by aggregation during regeneration.

Morphological and structural characteristics were examined using transmission electron microscopy (TEM) and scanning electron microscopy (SEM). TEM micrographs revealed the presence of multiple crystalline phases, including Fe_4N, $Fe_{16}N_2$, and α-Fe, as well as Si_3N_4 in the milled Si_3N_4/FeN* system (Supplementary Fig. 15). Notably, Si_3N_4/FeN* exhibited a higher degree of structural defects and lattice distortions than unpromoted FeN*. The crystalline Fe_4N phase was observed within the defective amorphous Fe surface in Si_3N_4/FeN*. SEM imaging and elemental mapping revealed that the milled Si_3N_4/FeN* system possessed a more uniform particle size distribution and enhanced elemental dispersion than FeN* (Supplementary Fig. 16). The combination of increased structural defects observed with TEM, and the improved dispersion observed with SEM analyses, suggests that as a physical promoter the Si_3N_4 contributed significantly to the morphology of the re-Si_3N_4/Fe catalyst. The Si_3N_4 promoter likely generated high-density defects and increased surface area, and thus enhanced overall catalytic performance.

X-ray photoelectron spectroscopy (XPS) was conducted to elucidate the chemical states of the materials (Fig. 3b). Si_3N_4/FeN* was determined to have a higher proportion of Fe_4N (396.6 eV, 37.3%) than $Fe_{16}N_2$ (397.2 eV, 31.8%), while the FeN* predominantly exhibited $Fe_{16}N_2$ content (397.5 eV, 67.1%) (Supplementary Fig. 17)[35]. The enhanced nitrogen content can be attributed to the high-density defects induced by Si_3N_4. The lower binding energy results in a higher surface electron density, thereby providing more favorable conditions for hydrogenation. Minor surface oxidation was also observed, likely due to sample handling, despite storage in a glovebox (Supplementary Figs. 17 and 18)[36,37]. Post-hydrogenation analysis revealed the peak shifted toward higher binding energies. This peak shift could be ascribed to the interaction between nitrogen and hydrogen, potentially resulting in the formation of NH_x*

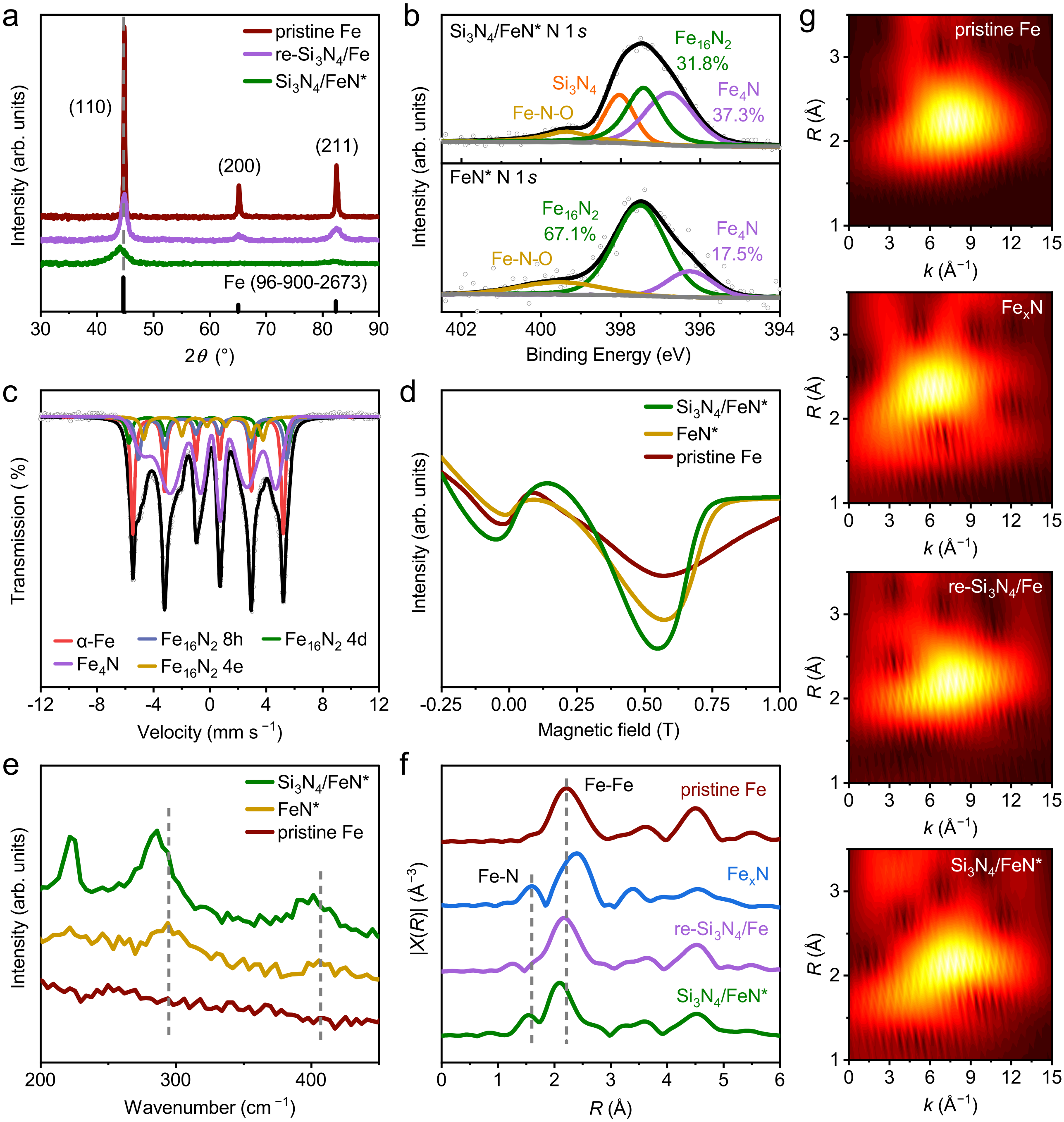

Fig. 3 | Defect mediated catalyst characterization. **a** XRD patterns of N_2 adsorbed Si_3N_4/FeN* and regenerated Si_3N_4/Fe in comparison with pristine Fe. **b** High-resolution XPS N 1*s* spectrum of Si_3N_4/FeN* and re-Si_3N_4/Fe powders. **c** Mössbauer spectra of Si_3N_4/FeN* at room temperature. **d** ESR and **e** Raman spectra of pristine Fe and nitrogenated Fe (FeN*) powders. **f** EXAFS spectra of pristine Fe, commercial Fe_xN ($x = 2$–4), re-Si_3N_4/Fe, and Si_3N_4/FeN*. **g** Corresponding wavelet transform analyses.

intermediates. The protonation of nitrogen during hydrogenation alters the electron density distribution.

Mössbauer spectroscopy was utilized to elucidate the active phases of the catalyst systems, capitalizing on its exceptional sensitivity to Fe. The resultant spectra revealed that Si_3N_4/FeN* consisted of a heterogeneous mixture of amorphous Fe_4N (52.3%), $Fe_{16}N_2$ (25.5%), and α-Fe (22.2%) (Fig. 3c). Notably, the $Fe_{16}N_2$ exhibited three distinct coordination environments (4 d, 8 h, 4e) that differed based on the Fe-N bond lengths. In an ideal scenario, the site occupancy ratio should be 1:2:1[38]. The analyzed ratio closely approximated this ideal ratio (Supplementary Tables 1, 2). In contrast, the proportions of $Fe_{16}N_2$ (29.6%) and α-Fe (33.0%) were higher in FeN* compared to Si_3N_4/FeN*, but Fe_4N (37.4%) was still the predominant phase (Supplementary Fig. 19). The $Fe_{16}N_2$ site ratio in FeN* also approached the ideal 1:2:1 distribution. The presence of Si_3N_4 favored the formation of Fe_4N, which is known to be more active for hydrogenation into ammonia.

Electron spin resonance (ESR) and Raman spectroscopy analyses demonstrate that the physical promoter Si_3N_4 induced an increased defect density within the catalyst structure. ESR analysis revealed that Si_3N_4/FeN* displays a significantly enhanced signal intensity compared to both pristine Fe and FeN* (Fig. 3d). This progressive intensification of the ESR signal provides compelling evidence that the addition of

Si_3N_4 generates supplementary defect sites, enhancing nitrogen adsorption through the redistribution of electron spins across the Fe surface. Complementing these findings, the Raman spectrum associated with the Fe phase exhibited asymmetrically broadened peaks, indicative of iron nitride phases in both Si_3N_4/FeN* and FeN*, which were not present in pristine Fe (Fig. 3e)[39]. Notably, a characteristic peak in the spectrum of Si_3N_4/FeN* was observed to redshift, which is attributed to strain within the Fe lattice. The strain weakens Fe-Fe bonds and creates coordinatively unsaturated Fe sites. Such lattice distortions significantly modify the d-band center of transition metal catalysts, bringing it closer to the Fermi level and thereby enhancing reactivity toward N_2 activation. This enhanced interaction can facilitate back-donation from Fe d-orbitals to the π^* antibonding orbitals of N_2.

Extended X-ray absorption fine structure (EXAFS) spectroscopy (Fig. 3f) revealed structural changes in the Fe-based catalyst systems with/without Si_3N_4 promotion. Si_3N_4/FeN* shows a distinct Fe-N peak at 1.54 Å. Notably, the Fe-Fe peak (2.1 Å) for Si_3N_4/FeN* shifted to lower *R*-value than the pristine Fe (2.2 Å), suggesting lattice contraction despite nitrogen incorporation. This unexpected phenomenon likely resulted from mechanochemically induced high-density defects and lattice distortions, promoting metastable Fe-N phases. Wavelet transform analysis (Fig. 3g) complemented these findings by providing a 2D representation of the *R*-space and *k*-space information. Si_3N_4/FeN* exhibited Fe-N interactions at higher *k* values (4.5 $Å^{-1}$) than Fe_xN (where $x = 2–4$, 3.1 $Å^{-1}$), indicating its stronger Fe-N bonding. The Fe-Fe scattering path in the nitrogen-adsorbed catalyst shifts to a lower *k* value (7.6 $Å^{-1}$) relative to the pristine Fe (7.8 $Å^{-1}$), consistent with the observed Fe-Fe bond contraction. These results collectively support the formation of unique Fe-N structures and highlight the structural changes induced by mechanochemistry.

Hydrogen dissociation analyses

Although pure Si_3N_4 itself did not show good reactivity (Supplementary Fig. 23), we assumed that Si_3N_4 also enhanced hydrogen adsorption by Fe during hydrogenation step in mechanochemistry because the amount of hydrogen uptake increased as the amount of Si_3N_4 increased. The hydrogen temperature programmed reduction (H_2-TPR) profiles provided compelling evidence (Fig. 4a). Si_3N_4/FeN* exhibited a prominent reduction peak at a substantially lower temperature (369 °C) than the FeN* (437 °C), indicating improved reducibility and accessibility of active sites. This shift towards a lower reduction temperature suggests that Si_3N_4 facilitated the dissociative adsorption of hydrogen molecules, potentially lowering the activation energy for the second hydrogenation step. It is noteworthy that the inset graph revealed the complex reduction behaviors of Si_3N_4/FeN* in the temperature range of 100–300 °C. These multiple reduction steps in the low-temperature region indicated a synergistic effect between Si_3N_4 and Fe, creating an optimal surface environment that could promote efficient hydrogen dissociation.

To further clarify the catalyst behavior in hydrogen atmosphere, temperature programmed desorption mass spectroscopy (TPD-MS) profiles were conducted. The H_2-TPD profile of the re-Si_3N_4/Fe catalyst exhibited two distinct desorption peaks at 227 and 454 °C, indicating the presence of multiple hydrogen adsorption sites with different binding energies (Fig. 4b). This heterogeneity in adsorption sites suggests that Si_3N_4 creates a more diverse surface landscape[40], potentially facilitating the dissociative adsorption of H_2 molecules and their subsequent reaction into ammonia. Moreover, the significant increase in peak intensities in re-Si_3N_4/Fe implies a higher concentration of active sites and improved surface area utilization (Supplementary Fig. 24). This result matched XPS and ESR spectra well.

The mechanistic pathway of hydrogen dissociation and incorporation was further elucidated through time-of-flight secondary ion mass spectrometry (TOF-SIMS) analysis. The re-Si_3N_4/Fe system exhibited MS signals for $FeNH^+$ (m/z 70.9) and $FeNH_2^+$ (m/z 71.9) species (Fig. 4c–f), accompanied by $SiNH^+$ (m/z 43.0) and $SiNH_2^+$ (m/z 44.0) intermediates (Supplementary Fig. 25), suggesting a cooperative hydrogen activation mechanism involving both Fe and Si_3N_4 interfaces. In contrast, the re-Fe catalyst demonstrated weaker signals for analogous $FeNH_x^+$ species. The substantially higher emission of NH_4^+ species (m/z 18.0) observed in re-Si_3N_4/Fe relative to re-Fe provided compelling evidence for enhanced hydrogen activation and ammonia formation in the hybrid catalyst system. The presence of both $SiNH_x^+$ intermediates alongside the enhanced $FeNH_x^+$ signals demonstrates a synergistic effect, where Si_3N_4 facilitates H_2 dissociation on Fe sites and mediates its transport to reaction centers. The corresponding 2D chemical maps visualized efficient successive hydrogenation progression in re-Si_3N_4/Fe.

Theoretical study

To elucidate the atomic-level effects of physical promoters on NH_3 synthesis, DFT calculations were conducted on the surface of Fe catalyst systems with three types of physical promoters: SiO_2, SiC, and Si_3N_4, as investigated in the experiments (Fig. 2a). At high temperatures, the RDS of ammonia synthesis is typically the N_2 dissociation step. However, at low temperatures, as in our experimental setup, the RDS shifts to the hydrogenation step because of strong H* adsorption on Fe surfaces, which readily blocks catalytic active sites[19]. Based on this, we evaluated both N_2 dissociation and hydrogenation reactions, with a higher focus on hydrogenation. When evaluating the energy barriers for N_2 dissociation on the Fe(110) catalyst surface with these promoters, minimal changes were observed compared to the clean Fe(110) surface (Supplementary Fig. 27). Similarly, the hydrogenation of N* into NH_3 showed only marginal variations in energy barriers at the RDS. This indicates that the overall impact of these physical promoters on the catalytic activity of the clean Fe(110) surface is negligible.

However, the primary role of physical promoters is the significant comminution of catalyst particles, driven by the high hardness of the promoters, which leads to the creation of more defective surfaces. In our previous work[19], we demonstrated that Fe catalysts with surface defects, such as vacancies or adatoms, exhibited reduced energy barriers for N_2 dissociation. Furthermore, it has been reported that the Fe(211) surface, characterized by a corrugated geometry, has a lower energy barrier for N_2 dissociation[41,42], and that the N* hydrogenation process leading to NH_3 formation is also accelerated on this surface (Supplementary Fig. 28). These findings suggest that surface defects play a crucial role in lowering reaction energy barriers. Therefore, we extended our study to include defective surface models that could be induced by the physical promoters, focusing on vacancies and adatoms due to their high feasibility.

Although adatoms are more readily formed than vacancies on the clean Fe(110) surface, vacancy formation becomes energetically more favorable when surface-adsorbed promoters are present. This results from the strong interaction between the Fe surfaces and promoter clusters, which weakens the bonds between Fe surface atoms (Supplementary Table 4). This effect is particularly pronounced for SiC and/or Si_3N_4 promoters.

DFT calculations in this work also reveal that defective Fe (Fe_d) surfaces with SiO_2 or Si_3N_4 promoters, denoted as SiO_2/Fe_d or Si_3N_4/Fe_d, respectively, exhibit lower energy barriers for both N_2 dissociation and N* hydrogenation compared to the clean Fe(110) surfaces (Supplementary Fig. 29). This is attributed to the stronger interaction between the Fe_d surface and the promoters (Supplementary Fig. 30). The promoter effect persisted in the system with a larger cluster (Si_6N_8), verifying that the small-sized model reflects its essential role and suggesting comparable trends could be expected for even larger nanoclusters (Supplementary Fig. 31). However, the SiC promoter does not significantly lower these barriers, consistent with our experimental results (Fig. 2a).

According to our DFT calculations, Si_3N_4 is the most effective promoter, significantly reducing the energy barriers for both N_2

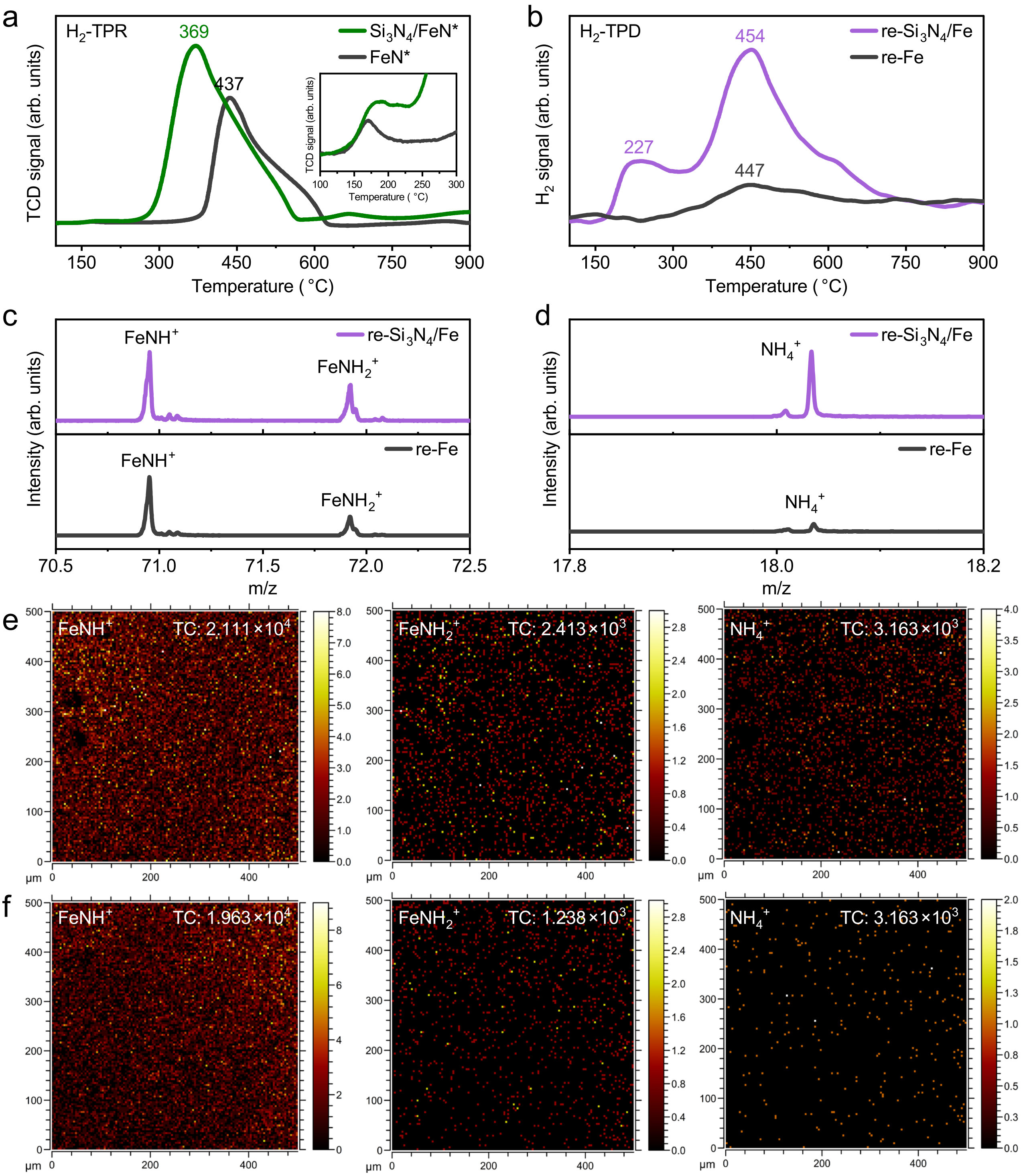

Fig. 4 | Hydrogen dissociation analyses. a H_2-TPR profiles for Si_3N_4/FeN* and FeN* powders. **b** H_2-TPD-MS analyses of pre-hydrogenated samples. TOF-SIMS MS signals of hydrogenation intermediates of **c** $FeNH^+$ and $FeNH_2^+$ and **d** NH_4^+. Corresponding 2D chemical maps of **e** re-Si_3N_4/Fe and **f** re-Fe. TC refers to total counts, which represents the sum of all detected secondary ion signals at each pixel.

dissociation (0.40 eV) and the hydrogenation steps at the RDS (1.29 eV) (Fig. 5a, b, Supplementary Table 5). Additionally, the Si_3N_4 promoter weakens hydrogen adsorption (Supplementary Table 6) and reduces the adsorbed hydrogen (H*) diffusion energy barrier by half, facilitating the diffusion of H* species to surface-bound N* species and ultimately enhancing NH_3 formation (Fig. 5c). The calculated reaction rate constants (Supplementary Fig. 32) and turnover frequencies (TOF, Fig. 5d and Supplementary Fig. 33) confirm the superior reaction kinetics of the Si_3N_4-promoted Fe (Si_3N_4/Fe) surface to the clean Fe(110) surface or the SiO_2 or SiC promoted Fe surfaces.

Moreover, Fe-N phases, such as Fe_4N and $Fe_{16}N_2$, which are likely formed after N* adsorption on the Fe catalyst (the first nitrogen dissociation step), significantly lower the energy barriers for the second and third hydrogenation steps of N* (Supplementary Fig. 34 and Supplementary Table 7). Although the clean $Fe_{16}N_2$ phase exhibits a

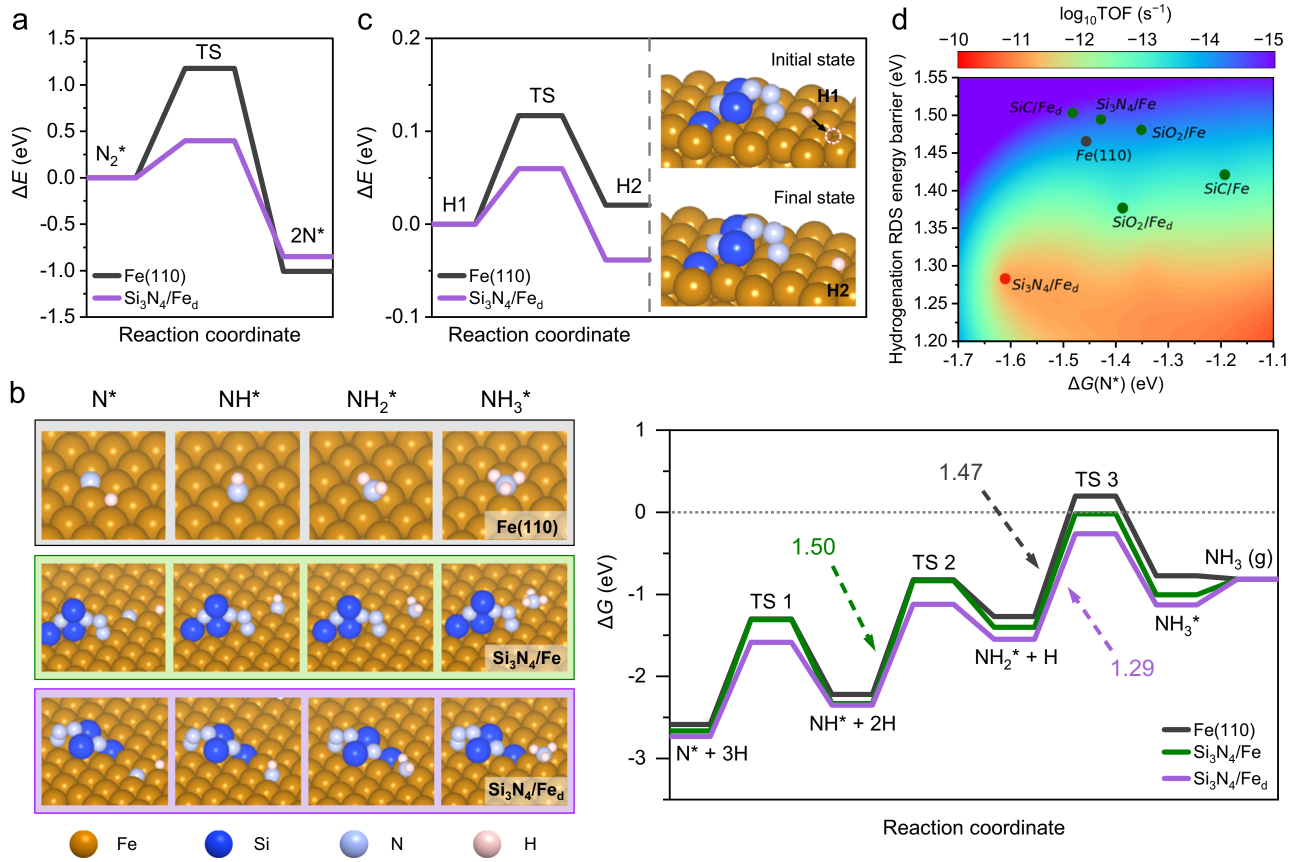

Fig. 5 | DFT calculations. a N_2 dissociation energy diagram of the Fe(110) and Si_3N_4/Fe_d surfaces. **b** Free energy changes of the N* hydrogenation to ammonia on the clean Fe(110) surface, a Si_3N_4 cluster on Fe surface (Si_3N_4/Fe), and Si_3N_4 cluster on defective Fe (Si_3N_4/Fe_d). Optimized geometries of N*, NH*, NH_2*, and NH_3* on the three different catalyst surfaces are shown with the graph. Color code: Fe—tan, Si—blue, N—light blue, and H—pink. **c** Comparison of the H* diffusion on the Fe(110) and Si_3N_4/Fe_d surfaces. **d** 2D activity heatmap describing the turnover frequency (TOF) from N* into ammonia.

relatively high RDS energy barrier for hydrogenation, the combination of a Si_3N_4 cluster and a surface vacancy on the Fe catalyst dramatically reduces the energy barrier. Experimentally, we observed that the presence of Si_3N_4 promoters led to an increased formation of Fe-N phases, such as Fe_4N and $Fe_{16}N_2$ (Fig. 3c and Supplementary Table 1), which further enhances catalytic efficiency in NH_3 synthesis. We additionally evaluated the effect of SiO_2 promoter on these phases, as SiO_2 also exhibited a higher ammonia production than that on clean Fe(110) (Fig. 2a). Our calculations showed that the use of SiO_2 lowers the hydrogenation energy barriers on both Fe_4N and $Fe_{16}N_2$ surfaces (RDS E_a: 1.23 eV for SiO_2/Fe_4N $_d$ and 1.21 eV for SiO_2/$Fe_{16}N_2$ $_d$) compared to the clean Fe_4N and $Fe_{16}N_2$ phases (Supplementary Fig. 35). However, these barriers remained slightly higher than those with the Si_3N_4 promoter, which explains the much higher ammonia yield with SiO_2 compared to that with the clean Fe(110), but still lower than that with Si_3N_4.

In summary, the Si_3N_4 promoter, with high hardness, enhances ammonia formation not only by increasing surface defects, but also by lowering the energy barriers for N_2 dissociation and N* hydrogenation, attributed to the strong interactions between Si_3N_4 clusters and the defective Fe (Fe_d) surface. Additionally, the improved hydrogen diffusion further accelerates the hydrogenation process. The influence of Si_3N_4 extends beyond the clean Fe catalyst surface, significantly enhancing the catalytic activity of the Fe_4N and $Fe_{16}N_2$ phases, which are more abundantly formed in the presence of the Si_3N_4 promoter, as demonstrated in our experiments.

Discussion

When the physical promoter was employed for mechanochemical ammonia synthesis, a synergistic effect was observed. The high hardness and abrasion resistance of the Si_3N_4 facilitated the generation of high-density defects and active sites on the Fe catalyst during ball-milling, thereby improving N_2 dissociation and H_2 activation kinetics. Moreover, Si_3N_4 acted as a dispersing agent, preventing catalyst agglomeration and maintaining a large area of active Fe surface. Our study provides a deeper understanding of the interplay between physical promotion and catalytic performance in mechanochemical ammonia synthesis, which could guide future research in developing more effective catalysts for various chemical processes.

Based on the results here, we anticipate that the mechanochemical approach, augmented by physical promotion, will provide significant advantages for new modes of ammonia synthesis in a hydrogen-based economy. The ability to conduct ammonia synthesis at lower temperatures and pressures could open avenues for decentralized, small-scale production facilities, which could be pivotal for the widespread adoption of ammonia as a hydrogen carrier. By enabling more efficient ammonia production, this mechanochemical methodology could play a vital role in overcoming the challenges associated with hydrogen storage and transportation, thereby facilitating the broader implementation of hydrogen-based energy systems and contributing to the development of sustainable energy infrastructure.

Methods

Chemicals and materials

High-purity silicon nitride powders, comprising β-phase (β-Si_3N_4, predominantly β-phase, ≤10 micron) and α-phase (α-Si_3N_4, predominantly α-phase, ≤10 micron), were supplied from Sigma-Aldrich. Additionally, iron (Fe) powder (iron sponge, -100 mesh, 99.9% metals basis), amorphous Si_3N_4 (am-Si_3N_4, silicon(IV) nitride, amorphous, nanopowder, 98.5 + %), β-phase silicon carbide (β-SiC, silicon carbide, beta-phase, 99% metals basis), silicon oxide (SiO_2, silicon(IV) oxide, 99.5% metals basis), potassium (K, potassium, chunks, in mineral oil, 98%), and iron nitride (Fe_xN, $x = 2–4$) were purchased from Alfa Aesar. To maintain the integrity of the materials, all chemicals were stored in an argon (Ar) atmosphere glove box (UNIlab pro, MBRAUN) with a purity of 99.999% (KOSEM Corp.). Mechanochemical experiments were conducted using a planetary ball-milling machine (Pulverisette 6, Fritsch) equipped with a hardened steel ball-milling jar (250 ml) and balls (Ø = 5 mm). All experiments using Si_3N_4 were conducted with β-Si_3N_4, unless specified. To ensure reproducibility, each experiment was independently repeated at least three times to determine the error bars.

Nitrogen dissociation kinetics

A mechanochemical experiment was conducted by loading 12.0 g of iron (Fe) catalyst and 0.9 g of Si_3N_4 into a hardened steel ball-milling jar with 500 g of steel balls in an Ar-filled glove box. The jar was then sealed and evacuated using a vacuum pump to remove any residual argon. Subsequently, high-purity nitrogen gas (N_2, 99.999%, KOSEM Corp.) was introduced into the jar at a pressure of 9 bar. The experiment was performed with 30 min of milling followed by a 10 min break to manage heat generation. This process was repeated for a total of 240,000 cycles to optimize the rotation speed for nitrogen adsorption. To determine the amount of adsorbed nitrogen, additional experiments were conducted at a milling speed of 450 r.p.m. for 5, 10, 15, 20, and 25 h, respectively. The pressure difference in the jar was measured using a pressure gauge, allowing for the calculation of the amount of adsorbed nitrogen.

Ammonia synthesis kinetics

Ammonia (NH_3) synthesis was performed via hydrogenation of the as-prepared Si_3N_4/FeN* and FeN* powders. Prior to hydrogenation, nitrogen adsorption was conducted at 450 r.p.m. for 20 h. Subsequently, the residual nitrogen gas in the jar was displaced with high-purity hydrogen gas (H_2, 99.999%, Daesung Industrial Gases Co.) using the same gas displacement method employed earlier for switching from argon (Ar) to nitrogen (N_2). The charged H_2 gas pressure was maintained at 9 bar. Because hydrogenation is an endothermic process, the hydrogenation cycle was implemented for 3 h, consisting of 60 min of milling followed by a 10 min break at a rotation speed of 500 r.p.m. After hydrogenation, the total gas pressure in the reactor was measured using a pressure gauge. Gas chromatography (GC, Agilent 7890B) was used to determine the gas concentration, allowing for the calculation of the amount of synthesized NH_3. To investigate the time dependence on NH_3 synthesis, the experiment was repeated seven times, with H_2 (9 bar) being recharged every 3 h. Finally, the powders were collected in an Ar-filled glove box to prevent surface oxidation.

Silicon-based promoter comparison

A total of 12.0 g of iron (Fe) powder was loaded into a stainless-steel ball-milling jar along with 500 g of stainless-steel balls. Subsequently, each silicon-based promoter, including Si_3N_4, β-SiC, or SiO_2, were added at a concentration of 3 at% with respect to Fe (0.03 × moles of Fe). The Fe powder and promoter was carefully handled and loaded into the ball-milling jar within an Ar-filled glove box to prevent contamination. The mechanochemical reaction was performed in two sequential steps. First, nitrogen dissociation was conducted by sealing the jar, evacuating residual argon using a vacuum pump, and introducing high-purity N_2 at a pressure of 9 bar. The ball-milling was performed at a rotation speed of 450 r.p.m. for 20 h, with a cycle of 30 min milling followed by a 10 min break to manage heat generation. After the nitrogen dissociation step, the pressure in the jar was measured using a pressure gauge to calculate the amount of dissociated nitrogen. For the subsequent hydrogenation step, the residual nitrogen gas was evacuated, and high-purity H_2 was introduced at a pressure of 9 bar. The hydrogenation was conducted at a rotation speed of 500 r.p.m. for 3 h, with a cycle of 60 min milling followed by a 10 min break. After hydrogenation, the total gas pressure in the reactor was measured using a pressure gauge, and gas samples were analyzed using GC to determine the concentration of synthesized NH_3.

Control and systematic experiments

Three control experiments validated the mechanistic role of Si_3N_4 in ammonia synthesis. First, to assess lattice nitrogen release, Si_3N_4 was ball-milled under H_2 atmosphere (9 bar) for 3 h without Fe catalyst at 500 r.p.m., yielding no detectable ammonia (<1 ppm). It confirms Si_3N_4 does not serve as a nitrogen source. Second, a blank test using Si_3N_4/Fe under 9 bar of Ar for 20 h at 450 r.p.m., followed by hydrogenation at 500 r.p.m. for 3 h in 9 bar of H_2. It verifies that atmospheric N_2 is essential for the reaction. Third, investigation of methane byproduct formation using high-purity iron balls (Fe 99.99%) was conducted N_2 dissociation for 20 h at 450 r.p.m. and 9 bar of N_2, and NH_3 synthesis for 3 h at 500 r.p.m. and 9 bar of H_2.

Promoter loading amount and phase effects

For studies on promoter loading amount effect, Fe powders (12.0 g) were loaded into a stainless-steel ball-milling jar, followed by the addition of β-Si_3N_4 at ratios ranging from 0.0 to 5.0 atomic percent (at %) to Fe. For studies on the Si_3N_4 phase effect, Fe powders (12.0 g) were loaded into a ball-milling jar along with 3 at% of each distinct Si_3N_4 phase, α-Si_3N_4, β-Si_3N_4, or amorphous Si_3N_4 (am-Si_3N_4). Nitrogen dissociation and hydrogenation were, respectively, carried out under 9 bar of N_2 for 12 h at 450 r.p.m. and 9 bar of H_2 for 5 h at 500 r.p.m., as was employed to determine the promoter loading amount effect. The phase effect studies were conducted under the same experimental conditions as the kinetic studies.

Chemical promoter comparison and stability test

To compare the performance of ammonia synthesis catalysts with different promoters, both the chemical promoter (K) and the physical promoter (Si_3N_4) were prepared under an inert atmosphere in an Ar-filled glove box to prevent contamination. Each promoter was used in equimolar quantities to ensure a consistent atomic basis for comparison, and for the catalytic experiments, either metallic K or Si_3N_4 was combined with 12.0 g of Fe powder and loaded into a steel jar. The experiments were conducted nitrogen dissociation followed by hydrogenation. Stability tests were performed over a series of 10 cycles, each cycle consisting of two sequential stages. Nitrogen dissociation at N_2 9 bar for 20 h, followed by hydrogenation at H_2 9 bar for 3 h.

Catalyst characterizations

The crystal structures of the samples were characterized by XRD using a D/max2500V instrument (Rigaku) with Cu-Kα radiation ($\lambda = 1.5418$ Å). The XRD patterns were recorded with a step size of 0.02° and a scan rate of $2°\ min^{-1}$. Mössbauer spectroscopy measurements were performed using a ^{57}Co (Rh) source at room temperature (Palacky University, 01216CN). The Mössbauer spectra were obtained in transmission geometry with a triangular velocity waveform. The isomer shifts of α-Fe were calibrated at room temperature. Hard X-ray absorption spectroscopy (XAS) measurements were conducted at the 6D UNIST-PAL beamline in the Pohang Accelerator Laboratory (South Korea). The XAS data were analyzed using Athena software. The morphology of the samples was characterized by field emission scanning electron microscopy (FE-SEM) using a Nova NanoSEM (FEI company) and a spherical-aberration-corrected transmission electron microscope (JEM-2100F, JEOL) for high-resolution atomic imaging.

XPS measurements were performed using a Thermo Fisher K-alpha XPS spectrometer in an Ar atmosphere glove box. The XPS spectra were deconvoluted using XPSPEAK41 software. The temperature-programmed reduction of hydrogen (H_2-TPR) was conducted on a chemisorption analyzer (Microtracbel, BELCAT II). The sample was heated from room temperature to 250 °C, maintained for 60 min in an Ar atmosphere, and then heated to 900 °C at 10 °C min^{-1} in a 5% H_2/Ar atmosphere. The released gases were continuously detected by a thermal conductivity detector. TPD-MS powders were pretreated using the same process, then gas adsorption was conducted at 100 °C for 60 min in a 5% desorption gas/helium (He) or Ar atmosphere. Subsequently, TPD-MS was conducted under He or Ar atmosphere. TOF-SIMS was performed using an ION-TOF GmbH instrument equipped with a 25 keV Bi^+ primary ion source and a 2 kV Cs^+ sputtering beam. Prior to TOF-SIMS analysis, the hydrogenated powders were compressed into 13 mm diameter pellets. All measurements were conducted in positive ion mode to identify and characterize the chemical species present.

Raman spectra were recorded using a DXR3 Raman microscope (Thermo Fisher Scientific) with a 532 nm laser excitation source at a power of 9 mW. ESR spectra were acquired using a Bruker EMXplus 9.5/12 spectrometer, fitted with an Oxford Instruments ESR900 cryostat. All measurements were performed at 295 K under non-saturating conditions. The spectrometer was operated at an X-band microwave frequency of 9.83 GHz, with a modulation frequency of 100 kHz, a modulation amplitude of 4.0 G, and a microwave power of 0.633 mW. N_2 adsorption-desorption isotherms were obtained using a BELSORP-max at 77 K over a relative pressure range of $P/P_0 = 10^{-6}$ to 0.99. Before the measurements, all samples were degassed under vacuum at 100 °C for 16 h to remove adsorbed impurities. The specific surface area of each sample was then calculated using the Brunauer-Emmett-Teller (BET) method.

Computational details

Spin-polarized density functional theory (DFT) calculations were performed using the Vienna Ab initio Simulation Package software[43,44] with the projector-augmented wave method[45]. The exchange-correlation energy was treated using the generalized gradient approximation using the revised Perdew-Burke-Ernzerhof[46] functional. A plane-wave energy cutoff of 500 eV was applied, and the Brillouin zone was sampled using a 2 × 2 × 1 Monkhorst-Pack k-point grid. During geometry optimization, all atoms in the top two layers, including adsorbates, were allowed to relax until reaching a force threshold of 0.05 eV $Å^{-1}$, with electronic self-consistency iteration convergence set to 10^{-5} eV. A smearing width of 0.05 eV was employed to account for partial occupancies, and the DFT-D3 method by Grimme et al.[47] was used to improve the description of long-range van der Waals interactions. Additionally, a dipole correction was applied along the z-axis. For the Fe–N phases, a Hubbard U correction was applied to the Fe 3 d orbitals using the approach of Dudarev et al.[48] to better account for localized electron correlation effects. Effective U values of 0.9 eV and 0.4 eV were used for $Fe_{16}N_2$ and Fe_4N, respectively[49,50].

The Fe surface model was cleaved from an optimized Fe bulk crystal along the (110) plane, resulting in a slab measuring 11.48 Å × 12.17 Å × 6.09 Å, with a 20 Å vacuum layer separating periodic images. During geometry optimizations, the top two layers were free to relax, while the bottom two layers were held fixed. Free energy for each reaction intermediate was calculated using the following equation:

$$\Delta G = \Delta E_{\mathrm{DFT}} + \Delta ZPE - T\Delta S \tag{1}$$

where ΔE_{DFT} is the DFT energy of each system, ΔZPE accounts for zero-point energy corrections, and $T\Delta S$ is to correct the entropy changes. The NIST web database[51] was used to calculate the ΔZPE and $T\Delta S$ of the gas-phase molecules.

Prior to modeling various physical promoters for NH_3 synthesis, USPEX[52] was employed to identify the most stable cluster structures of the promoters. The SiO_2 structure was sourced from the literature[53], where it has been extensively studied. However, due to the limited availability of studies on SiC and Si_3N_4 clusters, we utilized the USPEX code to determine their most stable geometries (Supplementary Notes and Supplementary Fig. 36). The physical promoters can induce defects on the catalyst surfaces; hence, we also evaluated the formation energies of defective surfaces such as vacancies and adatoms. The formation energies of these defective surfaces (E_f) were calculated with the following equation:

$$E_{\mathrm{f}} = E_{\mathrm{defective}} - E_{\mathrm{clean}} + \mathrm{n}\, E_{\mathrm{Fe}} \tag{2}$$

where $E_{\mathrm{defective}}$ represents the total energy of the defective surface model, E_{clean} is the total energy of the clean slab model without defects, n is the number of defects (positive for vacancies and negative for adatoms), and E_{Fe} is the energy of a single Fe atom calculated from the Fe bulk crystal.

The activation energies for N_2 dissociation and N* hydrogenation (* denotes a surface site) leading to ammonia were determined using the climbing image nudged elastic band[54] method. The transition states were verified through vibrational frequency analysis to ensure they exhibited only one imaginary frequency. The results were visualized using the VESTA software[55].

Data availability

The data generated in this study are provided in the Supplementary Information/Source Data file. Additional data can be obtained by contacting the corresponding author. All source data have been provided with this paper to ensure transparency and reproducibility of our results. Source data are provided with this paper.

References

1. Suryanto, B. H. R. et al. Nitrogen reduction to ammonia at high efficiency and rates based on a phosphonium proton shuttle. *Science* **372**, 1187–1191 (2021).
2. Li, W.-Q., Xu, M., Chen, J.-S. & Ye, T.-N. Enabling sustainable ammonia synthesis: from nitrogen activation strategies to emerging materials. *Adv. Mater.* **36**, 2408434 (2024).
3. Li, J., Xiong, Q., Mu, X. & Li, L. Recent advances in ammonia synthesis: from Haber-Bosch process to external field driven strategies. *ChemSusChem* **17**, e202301775 (2024).
4. Foster, S. L. et al. Catalysts for nitrogen reduction to ammonia. *Nat. Catal.* **1**, 490–500 (2018).
5. Mittasch, A. & Frankenburg, W. Early studies of multicomponent catalysts. in *Advances in Catalysis* Vol. 2 (eds Frankenburg, W. G., Komarewsky, V. I. & Rideal, E. K.) 81–104 (Academic Press, 1950).
6. Honkala, K. et al. Ammonia synthesis from first-principles calculations. *Science* **307**, 555–558 (2005).
7. Ye, D. & Tsang, S. C. E. Prospects and challenges of green ammonia synthesis. *Nat. Synth.* **2**, 612–623 (2023).
8. Li, G. et al. Research progress in green synthesis of ammonia as hydrogen-storage carrier under 'hydrogen 2.0 economy. *Clean. Energy* **7**, 116–131 (2023).
9. Collado, L. et al. Light-driven nitrogen fixation routes for green ammonia production. *Chem. Soc. Rev.* **53**, 11334–11389 (2024).
10. Aziz, M., Wijayanta, A. T. & Nandiyanto, A. B. D. Ammonia as effective hydrogen storage: a review on production, storage and utilization. *Energies* **13**, 3062 (2020).
11. Wan, Z., Tao, Y., Shao, J., Zhang, Y. & You, H. Ammonia as an effective hydrogen carrier and a clean fuel for solid oxide fuel cells. *Energy Convers. Manag.* **228**, 113729 (2021).
12. Du, H.-L. et al. Electroreduction of nitrogen with almost 100% current-to-ammonia efficiency. *Nature* **609**, 722–727 (2022).

13. Chen, W. et al. Emerging applications, developments, prospects, and challenges of electrochemical nitrate-to-ammonia conversion. *Adv. Funct. Mater.* **33**, 2300512 (2023).
14. Terlouw, T., Rosa, L., Bauer, C. & McKenna, R. Future hydrogen economies imply environmental trade-offs and a supply-demand mismatch. *Nat. Commun.* **15**, 7043 (2024).
15. Hasan, M. H. et al. A comprehensive review on the recent development of ammonia as a renewable energy carrier. *Energies* **14**, 3732 (2021).
16. Klerke, A., Hviid Christensen, C., K. Nørskov, J. & Vegge, T. Ammonia for hydrogen storage: challenges and opportunities. *J. Mater. Chem.* **18**, 2304–2310 (2008).
17. Chang, F., Gao, W., Guo, J. & Chen, P. Emerging materials and methods toward ammonia-based energy storage and conversion. *Adv. Mater.* **33**, 2005721 (2021).
18. Bora, N. et al. Green ammonia production: process technologies and challenges. *Fuel* **369**, 131808 (2024).
19. Han, G.-F. et al. Mechanochemistry for ammonia synthesis under mild conditions. *Nat. Nanotechnol.* **16**, 325–330 (2021).
20. Kim, J.-H. et al. Achieving volatile potassium promoted ammonia synthesis via mechanochemistry. *Nat. Commun.* **14**, 2319 (2023).
21. Tricker, A. W. et al. Mechanocatalytic ammonia synthesis over TiN in transient microenvironments. *ACS Energy Lett.* **5**, 3362–3367 (2020).
22. Lee, J. S., Han, G.-F. & Baek, J.-B. Mechanochemical ammonia synthesis: old is new again. *ChemSusChem* **16**, e202300459 (2023).
23. Reichle, S., Felderhoff, M. & Schüth, F. Mechanocatalytic room-temperature synthesis of ammonia from its elements down to atmospheric pressure. *Angew. Chem. Int. Ed.* **60**, 26385–26389 (2021).
24. He, C. et al. Mechanochemical synthesis of ammonia employing H2O as the proton source under room temperature and atmospheric pressure. *ACS Sustain. Chem. Eng.* **10**, 746–755 (2022).
25. Baláž, P. et al. Hallmarks of mechanochemistry: from nanoparticles to technology. *Chem. Soc. Rev.* **42**, 7571–7637 (2013).
26. Blackmore, R. H. et al. Understanding the mechanochemical synthesis of the perovskite LaMnO3 and its catalytic behaviour. *Dalton Trans.* **49**, 232–240 (2019).
27. Steenhaut, T., Grégoire, N., Barozzino-Consiglio, G., Filinchuk, Y. & Hermans, S. Mechanochemical defect engineering of HKUST-1 and impact of the resulting defects on carbon dioxide sorption and catalytic cyclopropanation. *RSC Adv.* **10**, 19822–19831 (2020).
28. Yin, H. & Du, A. Boosting nitrogen reduction activity by defect engineering in 2D iron monochalcogenides FeX (X=S, Se). *Small Struct.* **3**, 2200107 (2022).
29. Zhou, S. et al. Defect engineering in Ce-based metal–organic frameworks toward enhanced catalytic performance for hydrogenation of dicyclopentadiene. *ACS Appl. Mater. Interfaces* **16**, 38177–38187 (2024).
30. Fukuhara, M., Fukazawa, K. & Fukawa, A. Physical properties and cutting performance of silicon nitride ceramic. *Wear* **102**, 195–210 (1985).
31. Heath, G. A. et al. Research and development priorities for silicon photovoltaic module recycling to support a circular economy. *Nat. Energy* **5**, 502–510 (2020).
32. Ertl, G. & Huber, M. Interaction of nitrogen and oxygen on iron surfaces. *Z. Phys. Chem.* **119**, 97–102 (1980).
33. Ertl, G. Elementary steps in ammonia synthesis. In *Catalytic Ammonia Synthesis: Fundamentals and Practice* (eds Jennings, J. R.) 109–132. https://doi.org/10.1007/978-1-4757-9592-9_3 (Springer US, 1991).
34. Humphreys, F. J. & Hatherly, M. Grain growth following recrystallization. in *Recrystallization and Related Annealing Phenomena* 2nd edn (eds Humphreys, F. J. & Hatherly, M.) 333–378, Ch. 11. https://doi.org/10.1016/B978-008044164-1/50015-3 (Elsevier, 2004).
35. Jiang, Y., Zhang, X., Mehedi, A. A., Yang, M. & Wang, J.-P. A method to evaluate α″-$Fe_{16}N_2$ volume ratio in FeN bulk material by XPS. *Mater. Res. Express* **2**, 116103 (2015).
36. Torres, J., Perry, C. C., Bransfield, S. J. & Fairbrother, D. H. Low-temperature oxidation of nitrided iron surfaces. *J. Phys. Chem. B* **107**, 5558–5567 (2003).
37. Li, Z., Tang, G., Ma, X., Sun, M. & Wang, L. XPS study on chemical state and phase structure of PBII nitriding M50 steel. *IEEE Trans. Plasma Sci.* **38**, 3079–3082 (2010).
38. Ogawa, T. et al. Challenge to the synthesis of α″-$Fe_{16}N_2$ compound nanoparticle with high saturation magnetization for rare earth free new permanent magnetic material. *Appl. Phys. Express* **6**, 073007 (2013).
39. Zhang, Y., Xie, Y., Zhou, Y., Wang, X. & Pan, K. Well dispersed Fe_2 N nanoparticles on surface of nitrogen-doped reduced graphite oxide for highly efficient electrochemical hydrogen evolution. *J. Mater. Res.* **32**, 1770–1776 (2017).
40. Millar, G. J., Rochester, C. H., Bailey, S. & Waugh, K. C. Combined temperature-programmed desorption and fourier-transform infrared spectroscopy study of CO_2, CO and H_2 interactions with model ZnO/SiO_2, Cu/SiO_2 and $Cu/ZnO/SiO_2$ methanol synthesis catalysts. *J. Chem. Soc. Faraday Trans.* **89**, 1109 (1993).
41. Liu, D., Zhao, W. & Yuan, Q. Breaking the linear relation in the dissociation of nitrogen on iron surfaces. *ChemPhysChem* **23**, e202200147 (2022).
42. McKay, H. L., Jenkins, S. J. & Wales, D. J. Theory of $NH_x \pm H$ reactions on Fe{211}. *J. Phys. Chem. C.* **113**, 15274–15287 (2009).
43. Kresse, G. & Hafner, J. Ab initio molecular-dynamics simulation of the liquid-metal-amorphous-semiconductor transition in germanium. *Phys. Rev. B* **49**, 14251–14269 (1994).
44. Kresse, G. & Furthmüller, J. Efficient iterative schemes for ab initio total-energy calculations using a plane-wave basis set. *Phys. Rev. B* **54**, 11169–11186 (1996).
45. Blöchl, P. E. Projector augmented-wave method. *Phys. Rev. B* **50**, 17953–17979 (1994).
46. Hammer, B., Hansen, L. B. & Nørskov, J. K. Improved adsorption energetics within density-functional theory using revised Perdew-Burke-Ernzerhof functionals. *Phys. Rev. B* **59**, 7413–7421 (1999).
47. Grimme, S., Antony, J., Ehrlich, S. & Krieg, H. A consistent and accurate ab initio parametrization of density functional dispersion correction (DFT-D) for the 94 elements H-Pu. *J. Chem. Phys.* **132**, 154104 (2010).
48. Dudarev, S. L., Botton, G. A., Savrasov, S. Y., Humphreys, C. J. & Sutton, A. P. Electron-energy-loss spectra and the structural stability of nickel oxide: an LSDA+U study. *Phys. Rev. B* **57**, 1505–1509 (1998).
49. Stoeckl, P., Swatek, P. & Wang, J.-P. Magnetocrystalline anisotropy of α″–Fe16N2 under various DFT approaches. *AIP Adv.* **11**, 015039 (2021).
50. Blancá, E. L. P. y, Desimoni, J., Christensen, N. E., Emmerich, H. & Cottenier, S. The magnetization of γ′-Fe4N: theory vs. experiment. *Phys. Status Solidi B* **246**, 909–928 (2009).
51. Johnson, R. Computational Chemistry Comparison and Benchmark Database, NIST Standard Reference Database 101. National Institute of Standards and Technology https://doi.org/10.18434/T47C7Z (2002).
52. Lyakhov, A. O., Oganov, A. R., Stokes, H. T. & Zhu, Q. New developments in evolutionary structure prediction algorithm USPEX. *Comput. Phys. Commun.* **184**, 1172–1182 (2013).
53. Catlow, C. R. A. et al. Modelling nano-clusters and nucleation. *Phys. Chem. Chem. Phys.* **12**, 786–811 (2010).
54. Henkelman, G., Uberuaga, B. P. & Jónsson, H. A climbing image nudged elastic band method for finding saddle points and minimum energy paths. *J. Chem. Phys.* **113**, 9901–9904 (2000).

55. Momma, K. & Izumi, F. VESTA 3 for three-dimensional visualization of crystal, volumetric and morphology data. *J. Appl. Crystallogr.* **44**, 1272–1276 (2011).

Acknowledgements

This work was supported by the National Research Foundation of Korea (NRF) grant funded by the Korea government (MSIT): No. RS-2023-00221668 (J.S.L., S.-H.K., J.-H.B., J.-M.S., S.J.L., C.L., R.G., B.-J.J., G.-F.H., and J.-B.B.), RS-2024-00435493 (J.S.L., S.-H.K., J.-H.B., S.J.L., C.L., R.G., B.-J.J., and J.-B.B.), RS-2024-00466616 (J.S.L., S.-H.K., J.-H.B., S.J.L., C.L., R.G., B.-J.J., and J.-B.B.), RS-2024-00450102 (S.K. and S.S.H.). The XAFS experiments were performed in Pohang Accelerator Laboratory beamline (6D UNIST-PAL, South Korea).

Author contributions

J.S.L. and S.K. contributed equally to this work as co-first authors. J.-B.B., G.-F.H., and S.S.H. conceived the project and oversaw all the research phases. J.S.L. conducted experiments and characterizations. S.K. carried out DFT calculations. S.-H.K. reviewed data analyses, J.-H.B. performed TEM analyses, S.J.L. did surface area analyses, C.L., R.G., and B.-J.J. managed equipment and helped with data validation. J.-M.S. designed the figures. J.S.L., S.K., S.S.H., G.-F.H. and J.-B.B. co-wrote the paper, and all the authors commented on it.

Competing interests

The authors declare no competing interests.

Additional information

Supplementary information The online version contains supplementary material available at https://doi.org/10.1038/s41467-025-60715-3.

Correspondence and requests for materials should be addressed to Gao-Feng Han, Sang Soo Han or Jong-Beom Baek.

Peer review information *Nature Communications* thanks the anonymous reviewer(s) for their contribution to the peer review of this work. A peer review file is available.

Reprints and permissions information is available at http://www.nature.com/reprints